Pergamon

PII: S0301-9322(96)00058-4

Int. J. Multiphase Flow Vol. 23, No. 1, pp. 1–23, 1997

0301-9322/97 $17.00 + 0.00

UNSTEADY FLOW INTERACTIONS BETWEEN A PAIR OF ADVECTED VORTEX TUBES AND A RIGID SPHERE

I. KIM, S. ELGHOBASHI and W. A. SIRIGNANO

Department of Mechanical and Aerospace Engineering, University of California, Irvine, CA 92717, U.S.A.

(Received 2 February 1996; in revised form 20 August 1996)

Abstract—An idealized representation of the interaction of spherical particles with turbulent eddies of comparable length scale is considered by means of a three-dimensional, unsteady finite-difference Navier–Stokes solution of the interaction between a fixed rigid sphere and a pair of advecting vortex tubes. Initially the sphere is suddenly placed in the flow and held fixed in space. First, a doubly symmetric interaction with vortices of opposite rotation is considered. The resulting time-dependent drag differs from the drag in axisymmetric flows; however, the lift and torque on the sphere remain zero. Next, an interaction with two vortices of like rotation is studied. Here, non-zero lift and torque, as well as drag deviation from the axisymmetric case occur and would result in a deflection in the trajectory of a nonfixed sphere. The flow in this case behaves like that of a single vortex. Finally, a linear array of like-rotating vortices, interacting with a freely moving sphere, is considered. The two-dimensional deflection depends strongly upon the sphere/fluid density ratio and initial sphere Reynolds number. Lift and moment coefficients are shown to be linearly proportional to the maximum induced velocity due to the vortices. Moment coefficients are an order of magnitude less than lift coefficients. Copyright © 1996 Elsevier Science Ltd.

Key Words: unsteady flow over a sphere, sphere–vortex interaction

1. INTRODUCTION

The interactions between vortical structures and spherical particles or droplets is of primary practical interest in many particle-laden flows. These interactions modify the trajectories of individual particles and cause dispersion in a spray or cloud. Also, they can modify heat and mass transfer rates for the particles. There has been long-term interest in the effects of turbulent eddies which contain most the energy and whose sizes are orders of magnitude larger than the particle diameters. For example, extensive research has been performed to characterize the interaction between solid particles and turbulent shear flows (Chung and Troutt 1988; Crowe *et al.* 1988; Tang *et al.* 1992; Martin and Meiburg 1994).

However, a need exists to study the interactions of a particle with vortical structures that are smaller than, comparable in size to, or only a few times larger than the sphere. These small structures have the potential to produce the largest modifications to the boundary layer and near wake of the sphere. For example, our recent study (Kim *et al.* 1996) on the interaction between a spherical particle and a relatively large vortex (ratio of initial vortex diameter to particle diameter = 200) shows that the lift force on the particle due to a large vortex is much smaller than that due to a small vortex as will be shown in the present paper. Birouk *et al.* (1996) experimentally investigated turbulence effects on the vaporization of monocomponent single droplets in a chamber producing zero mean velocity, homogeneous isotropic turbulence. The largest eddy size in this experiment is five times the droplet diameter. They found that the turbulence strongly enhances droplet vaporization rates. However, the forces on the droplet were not measured.

In this paper, an idealized representation of those interactions is made by considering the viscous, incompressible, unsteady, three-dimensional flow associated with a pair of initially cylindrical vortex tubes advecting past the sphere. Initially the sphere is suddenly placed in the flow and held fixed in space. This study builds upon the previous study of Kim *et al.* (1995), hereafter identified as KES. In that paper, the authors examined the unsteady, three-dimensional interactions between a single advected cylindrical vortex tube and a fixed spherical particle whose diameter is of the same order of magnitude as the initial diameter of the vortex. That study served as a first step towards

better understanding the two-way interactions between small-scale turbulence and the particle. The extension to the case where there is sequential interaction with many eddies is straightforward; the results from the interaction with one eddy can be pieced together as time advances. Here we extend this work to study the interactions between a pair of advected vortex tubes and a stationary spherical particle. Clearly, the turbulence-particle interaction involves several eddies *simultaneously* influencing the particle and being influenced by the particle. For that reason, it is sensible to make the extension of this paper. The practical problem involves a wide variety of possible configurations, all of which cannot be covered in one study. We attempt to maximize the value of this study by considering both co-rotating and counter-rotating eddies and by varying the initial distance between the eddies.

In the earlier study (KES) the particle Reynolds number based on the freestream velocity and the particle diameter was in the range $20 \leqslant \mathrm{Re} \leqslant 100$. The initial size of the cylindrical vortex tube was in the range $0.25 \leqslant \sigma \leqslant 4$, where σ is the radius of the vortex tube normalized by that of the particle. We found that the maximum positive lift coefficient and the rms lift coefficient of the sphere are *linearly* proportional to the *circulation* of the vortex tube at small values of σ. However, at large values of σ, they are linearly proportional to the maximum induced velocity due to the vortex tube but *independent* of σ.

In the present paper, both co-rotating and counter-rotating vortical pairs are considered. In the counter-rotating case, only a symmetric configuration (see figure 1) is examined. Asymmetric configurations with counter-rotations are left for future studies. More attention is given to co-rotating pairs because they have the greatest effect on lift and torque. We expect, therefore, that deflections in the trajectories and dispersion of sprays and clouds will be greater in this case of co-rotation. The case of a 'train' of vortices advecting past the sphere at prescribed intervals is also examined.

Our specific objectives are to study:

(1) the detailed flow field behavior during interaction of a pair of vortex tubes with each other and with the sphere,
(2) the relationship between the lift coefficient of the sphere and the maximum induced velocity due to the two vortex tubes,
(3) the modification of the drag force caused by the interactions,
(4) the effects of Reynolds number, vortex size, and initial offset distance of the vortex, and
(5) the sphere deflection caused by the interaction with the vortices.

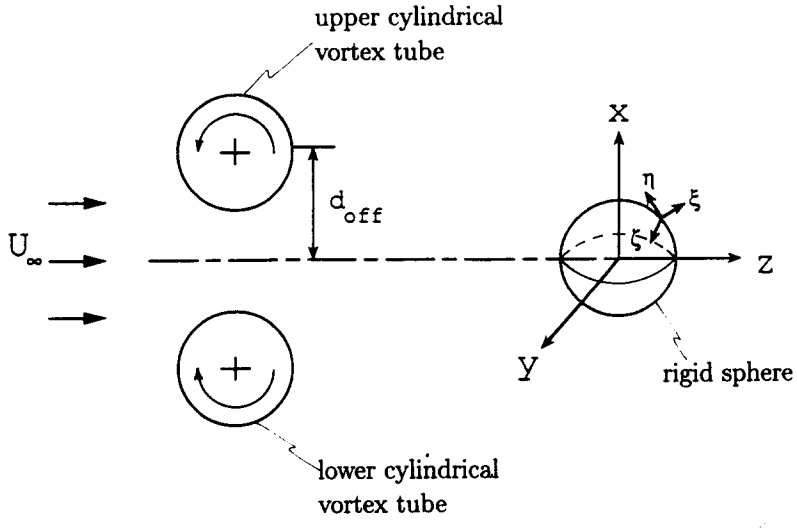

Figure 1. Flow geometry and coordinates: two counter-rotating cylindrical vortices are being advected toward a fixed sphere. x–z is the principal plane, and y–z is the reference plane.

The detailed study of the interactions between the particle and the unsteady velocity field provides fundamental information about the flow behavior that can be used in developing mathematical models for particle-laden flows. The next section provides a mathematical description of the flow considered, the governing equations, and the numerical solution procedure. Section 3 discusses the results including the numerical accuracy issues, the effects of varying the parameters listed above, and the trajectories of a moving spherical particle interacting with an array of vortex tubes of co-rotation as an extension of the results of KES and the present study. Section 4 provides a summary and concluding remarks.

2. PROBLEM STATEMENT AND FORMULATION

2.1. Flow description

Consider the time-dependent, three-dimensional, incompressible, viscous flow interactions between a pair of symmetric, initially cylindrical vortex tubes and a solid sphere. The vortex tubes are moving with the laminar free stream, and a sphere is suddenly placed and held fixed in space as shown in figure 1. The initial offset distance, d'_{off}, denotes the shortest distance between the initial vortical axis and the y–z plane which is parallel to the free stream. All the variables are nondimensionalized using the sphere radius a'_0 as the characteristic length and U'_∞ as the characteristic velocity, where the subscript $'$ denotes dimensional quantity. The two vortex tubes, having equal diameters of the order of the sphere diameter, are initially located 10 sphere radii upstream from the center of the sphere. The effects of the vortex tubes on the sphere are negligible at this initial distance because the magnitude of the initial velocity field induced by the vortex tubes is less than 2% of the free stream velocity. Far upstream, the flow is uniform with constant velocity $U'_\infty \mathbf{k}$ parallel to the y–z plane. There is one symmetry plane, the x–z plane, as seen in figure 1. A second symmetry plane (y–z) exists only when the two vortices have counter-rotations. Our general formulation does not take advantage of this second symmetry.

Note that, later in section 3.4, the fixed sphere results will be employed in a moving sphere trajectory analysis.

Two coordinate systems are used in our formulation following KES: the Cartesian coordinates (x, y, z) and the nonorthogonal generalized coordinates (ξ, η, ζ). The origin of the former coincides with the sphere center. ξ is the radial, η is the angular, and ζ is the azimuthal coordinates. The nonorthogonal generalized coordinate system can be easily adapted to three-dimensional arbitrary geometries. In the present study, a spherical domain is used, and the grid reduces to an orthogonal, spherical grid. The grids are denser near the surface of the spherical particle, and the grid density in the radial direction is controlled by the stretching function developed by Vinokur (1983). Due to symmetry, the physical domain is reduced to a half spherical space. The domain of the flow is bounded by $1 \leqslant \xi \leqslant N_1$, $1 \leqslant \eta \leqslant N_2$, $1 \leqslant \zeta \leqslant N_3$, where $\xi = 1$ and N_1 correspond, respectively, to the sphere surface and the farfield boundary surrounding the sphere; $\eta = 1$ and N_2 denote, respectively, the positive z-axis (downstream) and the negative z-axis (upstream); $\zeta = 1$ and N_3 refer, respectively, to the x–z plane in the positive x-direction and the x–z plane in the negative x-direction. Uniform spacing ($\delta\xi = \delta\eta = \delta\zeta = 1$) is used, for convenience, for the generalized coordinates.

The initial vortex tubes have a small core region with a radius σ (normalized by the sphere radius). This core is defined such that the initial velocity induced by the vortex tube approaches zero as the distance from the center of the vortex tube goes to zero, and at distances much greater than σ, the induced velocity approaches that of a point vortex. We use the vortex tube construction of Spalart (1982), which has the following stream function:

$$\psi_v(x, z, t = 0) = -\frac{\Gamma_j}{2\pi} \ln[(x - x_j)^2 + (z - z_j)^2 + \sigma^2],$$

where Γ_j is the nondimensional circulation around the vortex tube at radius σ and at the initial time. Γ_j is positive when the vortex tube rotates counterclockwise, and x_j and z_j denote the location of the center of the vortex tube. The circulation around a circular path far away from the center of the vortex is given by $\Gamma_{jt} = 2\Gamma_j$. Each vortex tube can be viewed as an evolution from the point

vortex due to the cylindrical viscous diffusion. The stream function for a pair of vortex tubes is given by

$$\psi_v(x, z, t = 0) = -\sum_{j=1}^{2} \frac{\Gamma_j}{2\pi} \ln[(x - x_j)^2 + (z - z_j)^2 + \sigma^2]. \quad [1]$$

2.2. Governing equations and boundary conditions

The continuity and momentum equations and the initial and boundary conditions are nondimensionalized using the sphere radius a_0' as the characteristic length and U_∞' as the characteristic velocity.

$$\nabla \cdot \mathbf{V} = \mathbf{0} \quad [2a]$$

$$\frac{\partial \mathbf{V}}{\partial t} + \nabla \cdot \mathbf{V}\mathbf{V} = -\nabla p + \frac{2}{\mathrm{Re}} \nabla^2 \mathbf{V}. \quad [2b]$$

The governing equations [2a] and [2b] are cast in terms of the generalized coordinates (ξ, η, ζ) to treat a three-dimensional body of arbitrary shape. The numerical integration is performed using a cubic computational mesh with equal spacing $(\sigma\xi = \delta\eta = \delta\zeta = 1)$.

The velocities on the sphere surface are zero due to the no-slip condition, and the pressure on the sphere is obtained from the momentum equation.

The boundary conditions are

$$\frac{\partial p}{\partial n} = \frac{2}{\mathrm{Re}} \frac{\partial^2 V_n}{\partial n^2}, \quad u = v = w = 0 \quad \text{at } \xi = 1, \quad [3a]$$

$$p = 0, \quad u = v = 0, \quad w = 1 \quad \text{at } \xi = N_1 \text{ and } N_{2\mathrm{mid}} \leqslant \eta \leqslant N_2 \text{ (upstream)}, \quad [3b]$$

$$p = 0, \quad \frac{\partial u}{\partial \xi} = \frac{\partial v}{\partial \xi} = \frac{\partial w}{\partial \xi} = 0 \quad \text{at } \xi = N_1 \text{ and } 1 \leqslant \eta \leqslant N_{2\mathrm{mid}} \text{ (downstream)}, \quad [3c]$$

$$\frac{\partial p}{\partial \zeta} = \frac{\partial u}{\partial \zeta} = \frac{\partial w}{\partial \zeta} = 0, \quad v = 0 \quad \text{at } \zeta = 1 \text{ and } N_3, \quad [3d]$$

where u, v, and w are the velocities in the x, y, and z direction, respectively, V_n is the velocity in the direction normal to the sphere surface, and p is the pressure. n denotes the direction normal to the sphere surface, $\partial/\partial n = \sqrt{\xi_x^2 + \xi_y^2 + \xi_z^2}\,\partial/\partial\xi$, and $\eta = N_{2\mathrm{mid}}$ denotes the mid-plane between $\eta = 1$ and N_2. Equation [3d] corresponds to the symmetry conditions and zero v velocity in the x–z symmetry plane. Conditions guaranteeing continuity in the η direction for p, u, v, and w on the axes $\eta = 1$ and $\eta = N_2$ are also imposed.

In order to start the numerical solution of [2a] and [2b], we provide initial velocity field by superposing the flow fields due to the uniform stream and the vortex tubes in addition to the no-slip condition on the sphere surface:

$$p_0 = 0, \quad u_0 = -\frac{\partial \psi_v}{\partial z}, \quad v_0 = 0, \quad w_0 = 1 + \frac{\partial \psi_v}{\partial x} \text{ except at } \xi = 1 \quad [4a]$$

$$p_0 = 0, \quad u_0 = v_0 = w_0 = 0 \quad \text{at } \xi = 1, \quad [4b]$$

where ψ_v is given by [1], respectively.

The initial pressure is estimated as zero over the whole computational domain. This estimation is corrected by the pressure correction equation and iteration procedure (see section 2.3 for details).

The only nondimensional groupings appearing in the equations and initial and boundary constraints are the sphere Reynolds number, vortex tube radius, offset distance, and vortex circulation (or vortex Reynolds number).

The equations evaluating the drag, lift, and moment coefficients are given in KES and thus will not be repeated here. The lift force is assumed positive when it is directed toward the positive x-axis.

Due to symmetry, only the y-component of the moment is non-zero and is assumed positive in the counter-clockwise direction.

2.3. *Numerical solution*

A three-dimensional, implicit, finite-difference algorithm has been developed to solve simultaneously the set of the discretized partial differential equations. The method is based on an alternating-direction-predictor-corrector (ADPC) scheme to solve the time-dependent Navier–Stokes equations. ADPC is a slight variation of alternating-direction-implicit (ADI) method and implemented easily when embedded in a large iteration scheme (Patnaik 1986; Patnaik *et al.* 1986). The control volume formulation is used to develop the finite-difference equations from the governing equations with respect to the generalized coordinates (ξ, η, ζ). One of the advantages of the control volume formulation is that mass and momentum are conserved over a single control volume, and hence the whole domain regardless of the grid fineness. An important part of solving the Navier–Stokes equations in primitive variables is the calculation of the pressure field. In the present work, a pressure correction equation is employed to satisfy indirectly the continuity equation (Anderson *et al.* 1984). The pressure correction equation is of the Poisson type and is solved by the successive-over-relaxation (SOR) method.

The overall solution procedure is based on a cyclic series of guess-and-correct operations. The velocity components are first calculated from the momentum equations using the ADPC method, where the pressure field at the previous time step is employed. This estimate improves as the overall iteration continues. The pressure correction is calculated from the pressure correction equation using the SOR method, and new estimates for pressure and velocities are obtained. This process continues until the solution converges at each time step. Overall convergence is achieved when the sum of the magnitudes of residuals of the pressure correction equation diminishes to about 10^{-6}. Since the initial guess for the pressure change is zero at every iteration, convergence of the pressure correction equation provides an indication that the overall convergence has been achieved.

3. RESULTS AND DISCUSSION

In sections 3.1 and 3.2, we discuss the three-dimensional interactions of a sphere and a pair of vortex tubes of counter-rotation. In section 3.3, we examine the three-dimensional interactions of a sphere and a pair of vortex tubes of co-rotation. In section 3.4, we investigate the trajectories of a moving sphere interacting with an array of vortex tubes of co-rotation.

Testing the accuracy of our numerical solution has been performed and discussed earlier in KES. The $51 \times 51 \times 51$ grid in a computational domain with an outer boundary located at 21 sphere radii from the sphere center is used in the following calculations. The run for the interaction between a single vortex tube and a sphere at Reynolds number 100 with the $51 \times 51 \times 51$ grid required 4.95 mega words, a dimensionless time step of $\Delta t = 0.002$, and a total time of 4 cpu h on Cray C-90 for the final time of $t_f = 24.5$. Each time step takes about 1.18 cpu s.

3.1. *Interactions of a sphere and a pair of vortex tubes with top-positive and bottom-negative circulations*

We consider the interactions of a pair of vortex tubes advected by the free stream and a sphere suddenly placed in the flow and held fixed in space. The two cylindrical vortex tubes are initially of the same size and rotating opposite to each other with top-positive and bottom-negative circulations as shown in figure 1. The y–z plane is half way between the two tubes so that the offset distance of one vortex tube is the negative of the offset distance of the other. The center of each vortex tube is located at 10 sphere radii upstream from x–y plane containing the center of the sphere. The base case calculation is that of Re = 100, $d_{off} = \pm 1.5$, and $\sigma = 1$.

Initially, each vortex tube has its maximum induced velocity v_{max} located at the edge of the core. Because the velocity and vorticity fields induced by one vortex tube influence those by the other, the total maximum induced velocity, v_{maxt}, due to the two vortex tubes depends on their size and separation distance and is in the range $0 \leqslant v_{maxt} \leqslant 2v_{max}$. The total maximum induced velocity v_{maxt} equals zero when $|d_{off}| = 0$, $2v_{max}$ when $|d_{off}| = \sigma$, and v_{max} when $|d_{off}| \gg 1$. For example, v_{maxt} is 0.738 for $v_{max} = 0.4$, $d_{off} = \pm 1.5$, and $\sigma = 1$. The base case calculation is that of Re = 100, $d_{off} = \pm 1.5$,

and $\sigma = 1$. Note that the lift and torque on the sphere are zero due to the flow symmetry in upper and lower regions of the sphere.

In order to describe the flow structure, we first consider the pseudo-streamlines and vorticity contours in the x–z symmetry plane, defined as the *principal plane*, where the strongest interactions occur between the vortical structures and the sphere. The y–z plane containing the front and rear stagnation points in the standard axisymmetric flow over a single sphere will be used as a reference plane (figure 1). We refer to the region above that plane as the 'upper' region and that below the plane as the 'lower' region.

The pseudo-streamlines are obtained from the pseudo-stream function which is defined by assuming that the velocity field in the principal (x–z) plane does not change in the direction normal to that plane and by using the two-dimensional stream function definition as follows

$$\psi_{ps}(r, \theta_0) = \psi_{ps}(r_0, \theta_0) + \int_{r_0}^{r} -u_\theta \, dr.$$

The sphere surface in the principal plane is used as a reference streamline ($\psi_{ps} = 0$). We note that a real stream function ψ cannot be defined and calculated from the velocity in the principal plane due to the existence of a divergence associated with the third component of velocity. Nevertheless, for descriptive purposes only, it is convenient to use the two-dimensional stream function definition to present descriptions of the flow pattern.

Figure 2(a)–(f) display the pseudo-streamlines (left column) and the contour lines of y-component vorticity (right column) in the principal plane at $t = 0$, 3, 6, 9, 12, and 15 for Re = 100, $d_{off} = \pm 1.5$, $\sigma = 1$ with $v_{maxt} = 0.738$ ($v_{max} = 0.4$). The contour values of the pseudo-streamlines are 0, ± 0.02, ± 0.1, ± 0.3. The contour values of the vorticity are ± 0.4, ± 0.8, ± 1.4, ± 2, with the highest magnitude at the sphere surface.

Comparing the vorticity contours in figure 2(a)–(f) with those of the single vortex tube in figure 5 of KES, we see that the two vortex tubes move downstream faster than the single vortex. This additional acceleration occurs because the velocity magnitude at the center of each vortex tube equals that of the base flow plus that induced by the other vortex tube.

The distance between the top pseudo-streamline and the bottom pseudo-streamline in figure 2(a)–(c) is narrower on the segment connecting the vortex tube centers than any other place along the stagnation pseudo-streamline. This indicates that the velocity near the middle of the segment between the vortex tube centers is higher than any other place along the stagnation pseudo-streamline. The induced velocity due to the vortex tubes is added to the base flow near the stagnation pseudo-streamline.

Figure 3 shows the drag coefficients of the sphere as a function of time for the same parameters as above. The drag coefficients are obtained with four different total maximum induced velocities due to the vortex tubes, $v_{maxt} = 0.185$, 0.369, 0.554, and 0.738 ($v_{max} = 0.1$, 0.2, 0.3, and 0.4). The temporal behavior of the drag coefficients is different from that of the case of the pair of vortex tubes of co-rotation as will be shown in section 3.3. The time-averaged value of the deviation of the drag coefficient from that of the axisymmetric flow past a sphere for all values of v_{maxt} is not negligible and increases linearly with v_{maxt}. The time-averaged drag coefficient $C_{D,ave}$ may be expressed by

$$C_{D,ave} = C_{D,axi} + \beta v_{maxt}, \qquad [5]$$

where the constant $\beta = 0.27$, and $C_{D,axi}$ is the time averaged value of the drag coefficient in the case of axisymmetric flow ($v_{maxt} = 0$). Equation [5] is accurate within 1.8%. The drag coefficients reach their maximum at about $t = 9$ (see figure 3). The maximum drag coefficient $C_{D,max}$ can be expressed approximately by [5] but with $\beta = 1.05$, and $C_{D,axi}$ here is the local value of the axisymmetric drag coefficient at the time of $C_{D,max}$. Because the top and bottom vortex tubes have positive and negative circulations, respectively, the induced velocity due to the vortex tubes adds its magnitude to the base flow along the stagnation pseudo-streamline. This increased velocity causes the pressure at the stagnation point and the shear stresses in the upper and lower left regions to be higher than those of the axisymmetric flow past a sphere. As a consequence, the drag is increased.

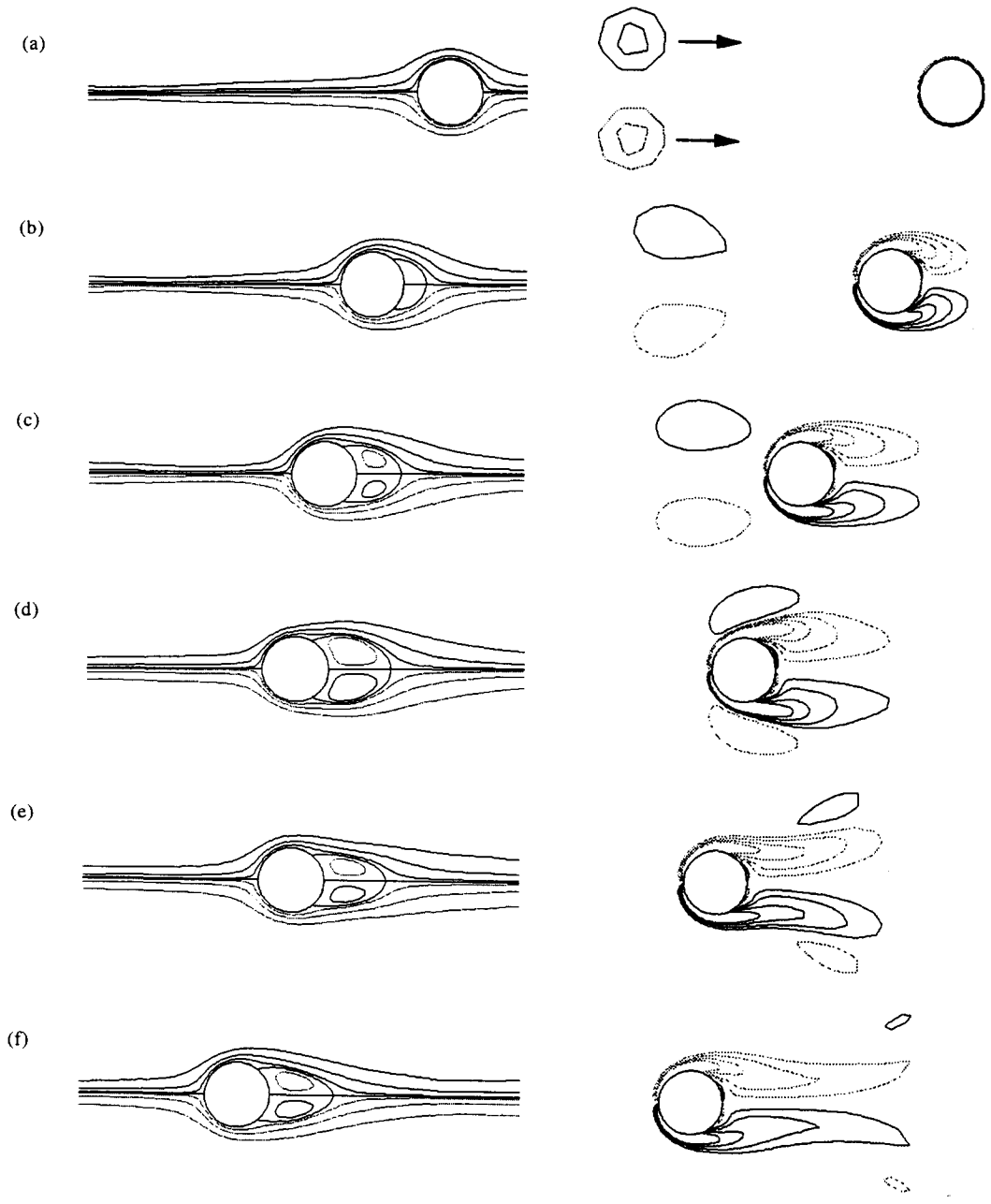

Figure 2. Pseudo-streamlines (left column) and contour lines of y-component vorticity (right column) in the principal plane at (a) $t = 0$, (b) 3, (c) 6, (d) 9, (e) 12, and (f) 15 for Re = 100, $d_{off} = \pm 1.5$, $\sigma = 1$, and $v_{maxt} = 0.738$, with top-positive and bottom-negative circulations.

3.2. Interactions of a sphere and a pair of vortex tubes with top-negative and bottom-positive circulations

We consider the same initial flow geometry and parameters as those in section 3.1 but for a pair of vortex tubes with top-negative and bottom-positive circulations.

Figure 4(a)–(f) display the pseudo-streamlines (left column) and the contour lines of y-component vorticity (right column) in the principal plane at $t = 0$, 3, 6, 9, 12, and 15 for Re = 100, $d_{off} = \pm 1.5$, $\sigma = 1$ with $v_{maxt} = 0.738$ ($v_{max} = 0.4$). The contour values of the pseudo-streamlines and the vorticity are the same as those in the previous section.

The vorticity contours in figure 4(a)–(f) show that the two vortex tubes move downstream slower than the single vortex tube in figure 5 of KES. This relative deceleration occurs because the velocity

magnitude at the center of each vortex tube equals that of the base flow minus that induced by the other vortex tube.

The distance between the top pseudo-streamline and the bottom pseudo-streamline in figure 4(a)–(c) is broader near the segment connecting the vortex tube centers than any other place along the stagnation streamline. This indicates that the velocity near the middle of the segment between the vortex tube centers is lower than those upstream or downstream of the vortex tubes along the stagnation streamline. The induced velocity due to the vortex tubes is subtracted from the base flow near the stagnation pseudo-streamline.

Figure 5 shows the drag coefficients of the sphere as a function of time for the same parameters as above. The drag coefficients are obtained for four different total maximum induced velocities due to the vortex tubes, $v_{maxt} = 0.185$, 0.369, 0.554, and 0.738 ($v_{max} = 0.1$, 0.2, 0.3, and 0.4). The temporal behavior of the drag coefficients is different from that of the case of the pair of vortex tubes of co-rotation as will be shown in section 3.3. The time-averaged value of the deviation of the drag coefficient from that of the axisymmetric flow past a sphere for all values of v_{maxt} is not negligible and decreases linearly as v_{maxt} increases. The time-averaged drag coefficient $C_{D,ave}$ may be expressed by [5] but with the proportionality constant $\beta = -0.28$, and $C_{D,axi}$ is the time-averaged value of the drag coefficient in the case of axisymmetric flow ($v_{maxt} = 0$). The drag coefficients reach their minimum at about $t = 11$ (see figure 5). The minimum drag coefficient $C_{D,min}$ can be expressed approximately by [5] but with $\beta = -0.95$, and $C_{D,axi}$ here is the local value of the axisymmetric drag coefficient at the time of $C_{D,min}$. Because the top and bottom vortex tubes have negative and positive circulations, respectively, the induced velocity due to the vortex tubes is subtracted from the base flow velocity along the stagnation streamline. This causes the pressure at the stagnation point and the shear stresses in the upper and lower left regions to be lower than those of the axisymmetric flow past a sphere. Thus, the drag is reduced.

3.3. Interactions of a pair of vortex tubes of co-rotation and a sphere

We consider the same initial flow geometry and parameters as those in section 3.1 but for a pair of vortex tubes of co-rotation. The base case calculation is that of Re = 100, $d_{off} = \pm 1.5$, and $\sigma = 1$.

Initially each vortex tube has its maximum induced velocity v_{max} located at the edge of the core. Because the velocity and vorticity fields induced by one vortex tube influence those by the other,

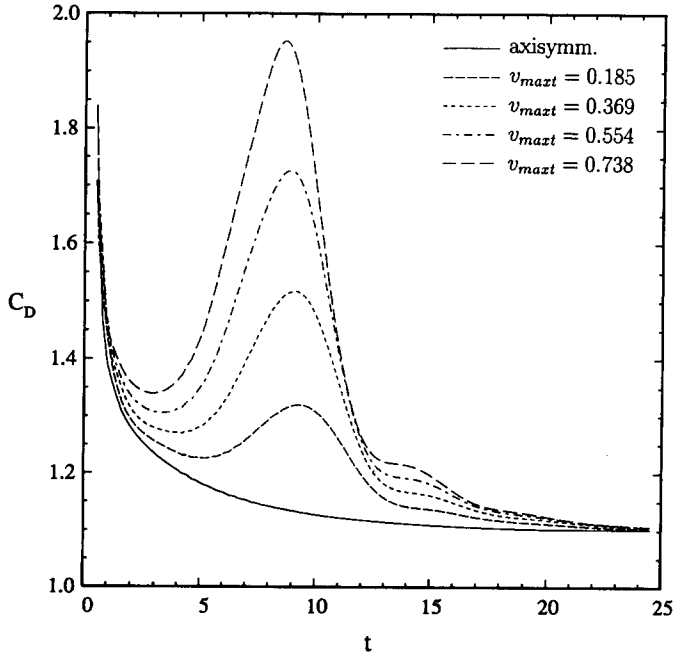

Figure 3. Drag coefficient of the sphere as a function of time and v_{maxt} for Re = 100, $d_{off} = \pm 1.5$, and $\sigma = 1$, with top-positive and bottom-negative circulations.

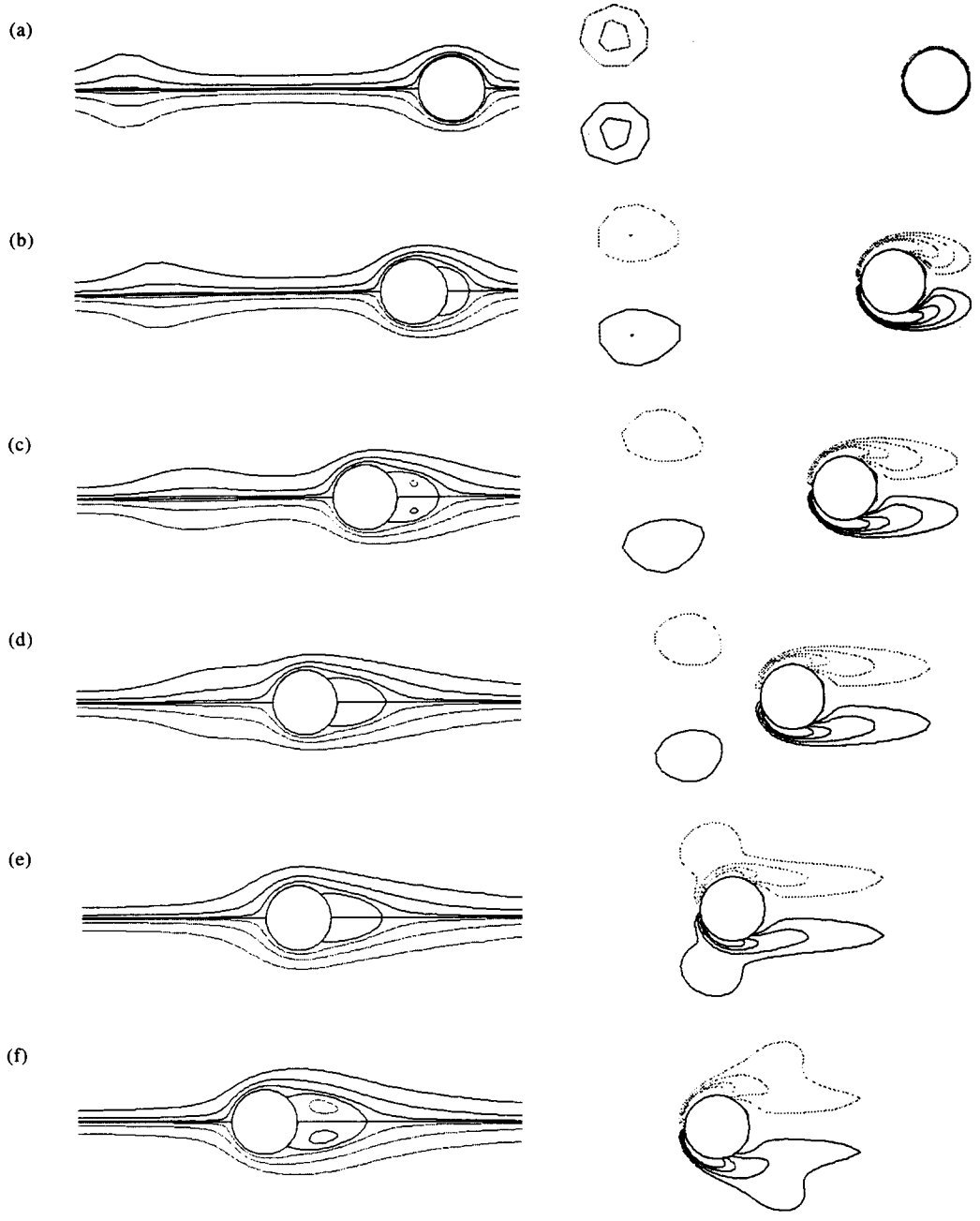

Figure 4. Pseudo-streamlines (left column) and contour lines of y-component vorticity (right column) in the principal plane at (a) $t = 0$, (b) 3, (c) 6, (d) 9, (e) 12, and (f) 15 for Re = 100, $d_{off} = \pm 1.5$, $\sigma = 1$, and $v_{maxt} = 0.738$, with top-negative and bottom-positive circulations.

the total maximum induced velocity, v_{maxt}, due to the two vortex tubes depends on their size and separation distance and is in the range $v_{max} \leqslant v_{maxt} \leqslant 2v_{max}$. v_{maxt} equals $2v_{max}$ when $|d_{off}| = 0$ and equals v_{max} when $|d_{off}| \gg 1$. For example, $v_{maxt} = 0.59$ for $v_{max} = 0.4$, $d_{off} = \pm 1.5$, and $\sigma = 1$.

In sections 3.3.1 and 3.3.2, we investigate the base case. In sections 3.3.3 and 3.3.4, we discuss the effects of the size and the offset distance of the vortex tubes and Reynolds number, respectively.

3.3.1. Flow structure. Figure 6(a)–(f) display the pseudo-streamlines (left column) and the contour lines of y-component vorticity (right column) in the principal plane at $t = 1$, 6, 10, 15, 21, and 30 for Re = 100, $d_{off} = \pm 1.5$, $\sigma = 1$, and $v_{maxt} = 0.59$ ($v_{max} = 0.4$). The contour values of the pseudo-streamlines are 0, ± 0.02, ± 0.1, ± 0.3. The contour values of the vorticity are ± 0.4,

± 0.8, ± 1.4, ± 2, with the highest magnitude at the sphere surface. The solid and dotted lines in the figures represent, respectively, positive and negative values.

The pseudo-streamlines shown in figure 6(a)–(f) resemble closely those for the interaction between a single vortex tube and a sphere which was described in KES. Since the description of the flow structure with the aid of the streamlines is given in KES, it will not be repeated here, and only the vorticity contours will be described here.

The vorticity contours in figure 6(a) and (b) show that the vortex tubes not only are advected downstream but also rotate about each other. The contour lines of vorticity in the figures also show that viscous diffusion takes place. It is well known that two co-rotating point vortices located a distance apart in an inviscid flow rotate with constant angular velocity about the point located at the center of the segment connecting them while the separation distance held fixed. On the other hand, when two co-rotating vortex tubes are located a distance apart in an inviscid flow and the separation distance is small enough, they interweave as well as rotate about each other (Zabusky *et al.* 1979; Overman and Zabusky 1982; Rangel and Sirignano 1989).

Figure 6(c) and (d) show that the vortex tubes contact the boundary layer of the sphere and go around the bottom of the sphere. The reason for the passage of the vortex tubes around the bottom of the sphere rather than around the top is as follows. When the vortex tubes rotating counter-clockwise come close to the sphere boundary layer, they augment the magnitude of the vorticity in the lower boundary layer and reduce that of the vorticity in the upper boundary layer. Consequently, the vorticity in the lower boundary layer induces a velocity in the downward direction at the location of the vortex tubes with higher magnitude than that induced by the vorticity in the upper boundary layer. This downward induced velocity advects the vortex tubes below the sphere (KES).

Figure 6(e) shows that the pairing vortex tubes merge into one vortex due to the interweaving and the viscosity. Figure 6(f) shows that the vorticity contours around the sphere approach that of the axisymmetric flow as the tubes are advected far downstream.

A three-dimensional view of the pair of vortex tubes is examined by considering the y-component of vorticity vector. Figure 7(a) and (b) show the views of a three-dimensional contour surface of $\omega_y = 0.2$ at $t = 6$ and 21, respectively, for the flow depicted in figure 6. The figures show a view looking down with an acute angle toward the y–z plane. The ellipse in the figures is the boundary of the spherical computational domain viewed at an angle. It appears as a circle when viewed

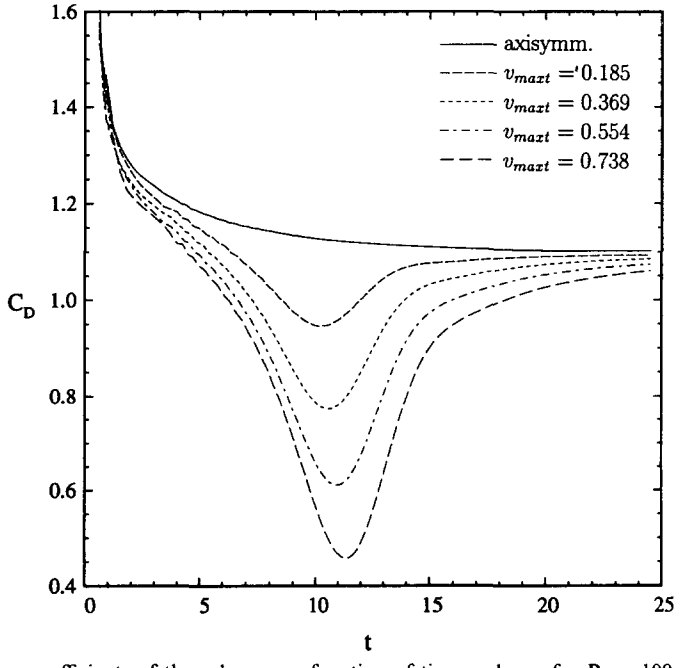

Figure 5. Drag coefficients of the sphere as a function of time and v_{maxt} for Re = 100, $d_{off} = \pm 1.5$, and $\sigma = 1$, with top-negative and bottom-positive circulations.

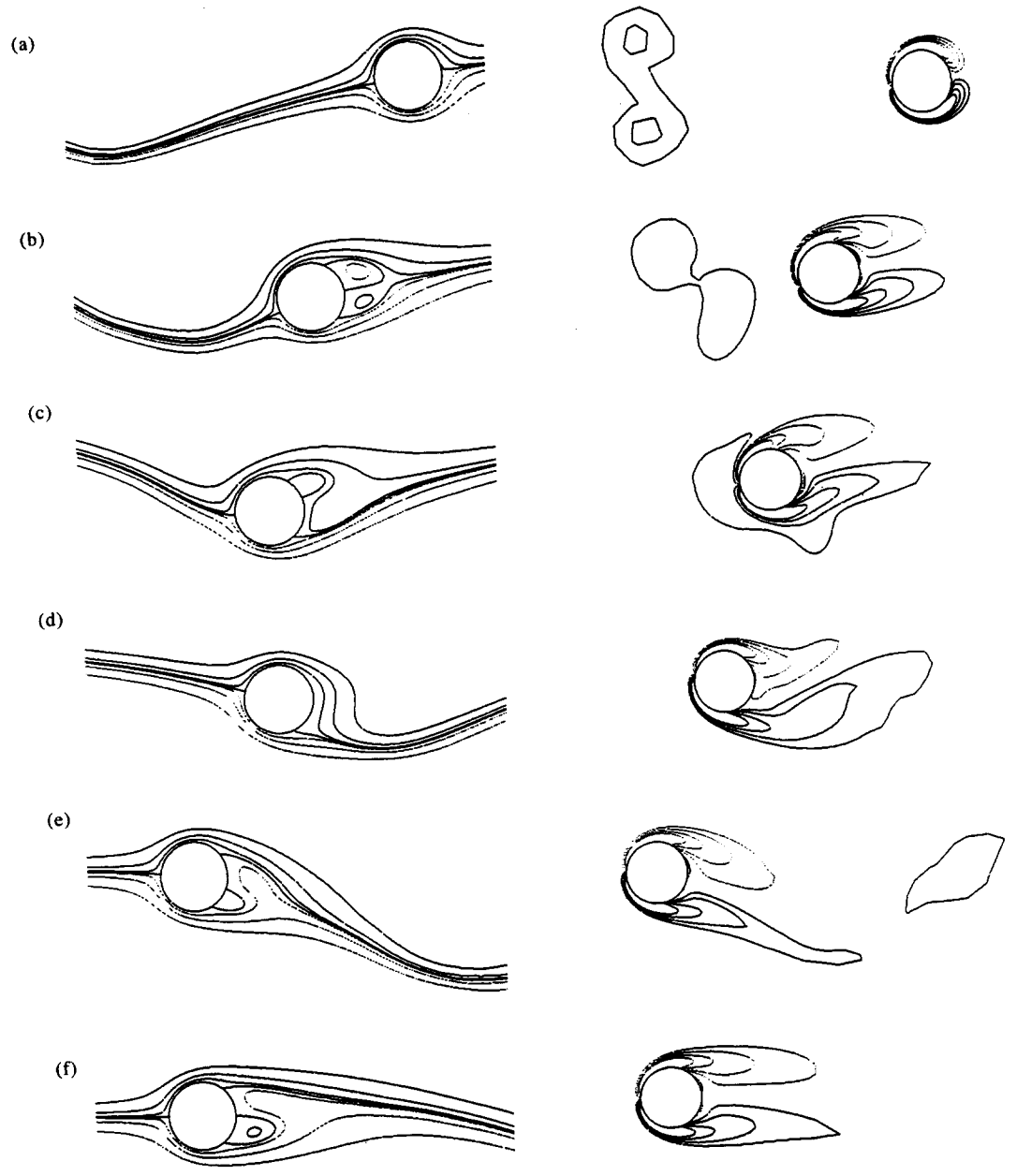

Figure 6. Pseudo-streamlines (left column) and contour lines of y-component vorticity (right column) in the principal plane at (a) $t = 1$, (b) 6, (c) 10, (d) 15, (e) 21, and (f) 30 for Re = 100, $d_{off} = \pm 1.5$, $\sigma = 1$, and $v_{maxt} = 0.59$.

normal to the principal plane. The sphere is at the center of the domain in figure 7(a) and (b). Figure 7(a) shows that the two vortex tubes rotate about each other. Figure 7(b) demonstrates that the pair of vortex tubes merge after some time.

The resemblance of the streamline pattern between the case of a pair of vortex tubes and the case of a single vortex tube indicates that the force and moment on the sphere due to a pair of vortex tubes may be close in value to those due to a single vortex tube. In the next subsections, we discuss the lift, moment, and drag coefficients for the pair of vortex tubes and compare them with those for a single vortex tube.

3.3.2. Lift, moment, and drag coefficients and effect of tube circulation. Figure 8 shows the lift coefficients of the sphere as a function of time for Re = 100, $d_{off} = \pm 1.5$, and $\sigma = 1$. The lift coefficients are computed for four different total maximum induced velocities v_{maxt} due to the pair of vortex tubes, with magnitudes equal to 0.148, 0.295, 0.443, and 0.590 ($v_{max} = 0.1$, 0.2, 0.3, and

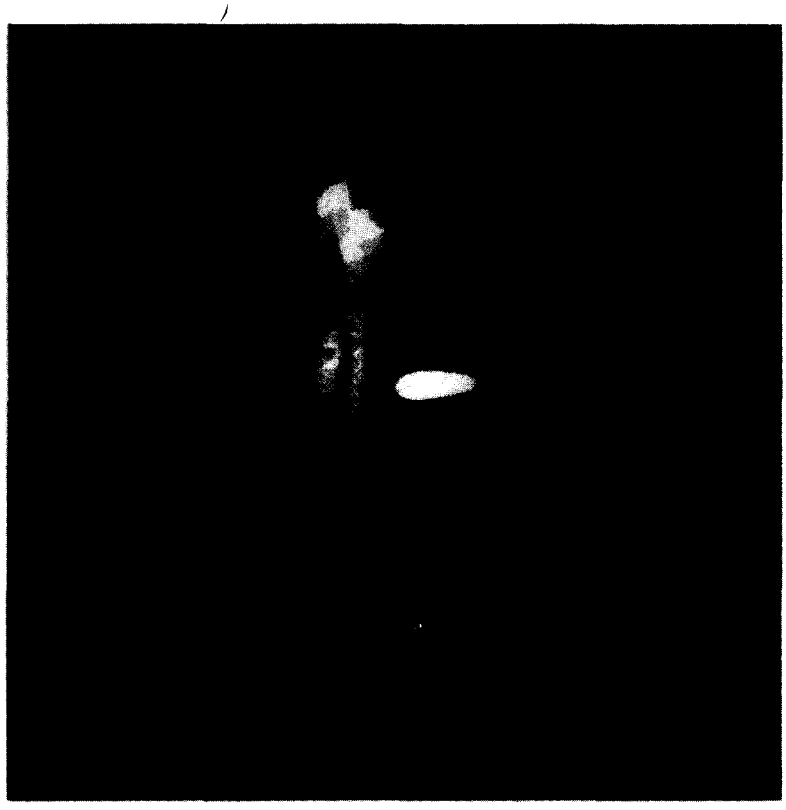

(a)

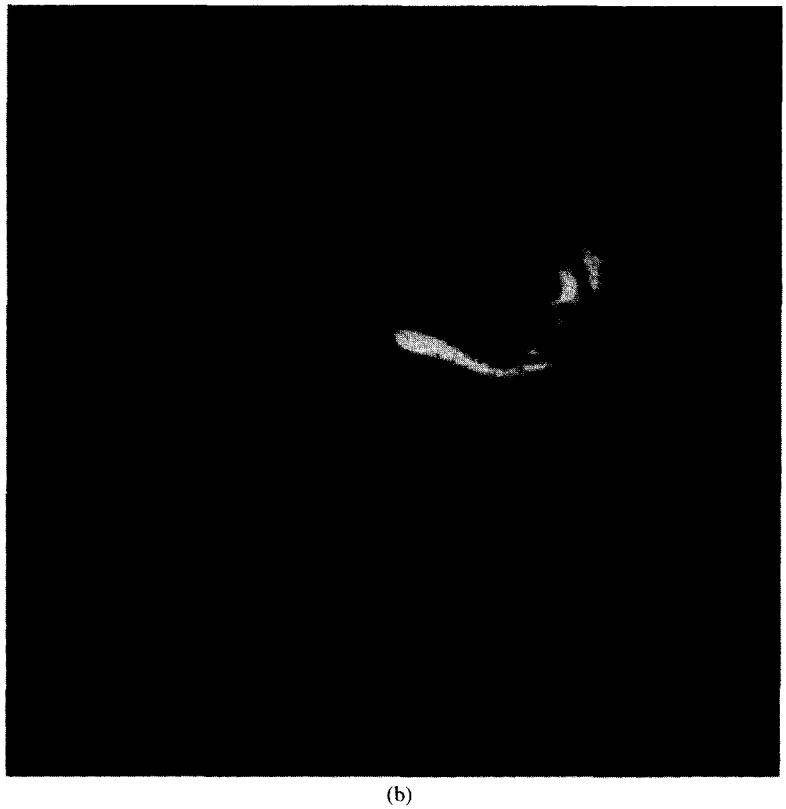

(b)

Figure 7. A view of three-dimensional contour surfaces of $\omega_y = 0.2$ at (a) $t = 6$ and (b) $t = 21$ for the flow depicted in figure 2.

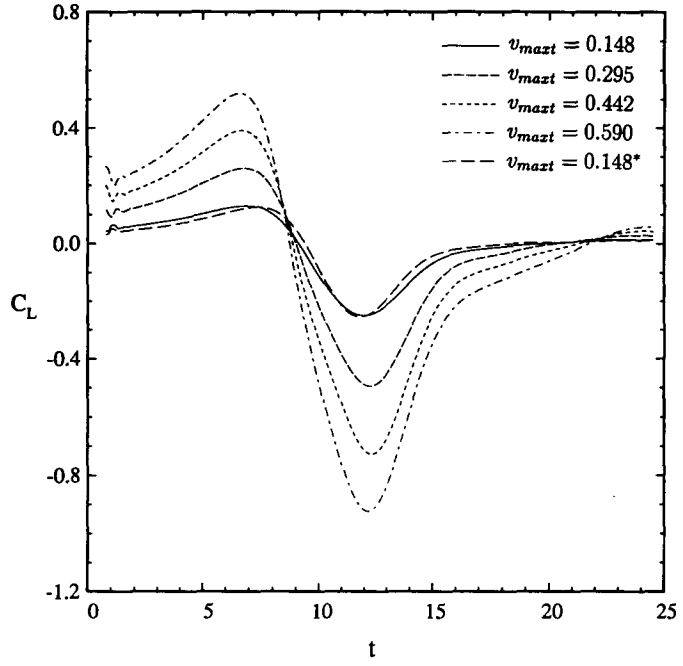

Figure 8. Lift coefficients of the sphere as a function of time and v_{maxt} for Re = 100, $d_{off} = \pm 1.5$, and $\sigma = 1$.

0.4) normalized by free stream velocity. Due to the sudden placement of the sphere into the stream, it takes a short time ($0 < t < 0.8$) for the initial flow perturbations to vanish.

When the pair of vortex tubes approach the sphere ($0 \leqslant t < 9$), they produce upwash resulting in a positive lift force on the sphere. The maximum positive lift coefficient $C_{L,max1}$ occurs at about $t = 6.8$. On the other hand, when the vortex tubes pass the sphere, they produce downwash and higher fluid velocity near the bottom of the sphere than the top due to the shear flow imposed by the vortex tubes resulting in a negative lift force. The magnitude of the negative lift is greater than the positive lift. The maximum negative lift coefficient $C_{L,max2}$ occurs at about $t = 12.2$. $C_{L,max1}$ and $C_{L,max2}$ are *linearly* proportional to the total maximum induced velocity. The maximum positive lift coefficient $C_{L,max1}$ is expressed by

$$C_{L,max1} = cv_{maxt}, \qquad [6]$$

where the proportionality constant $c = 0.88$. The maximum negative lift coefficient $C_{L,max2}$ is also expressed by [6] but with $c = -1.62$. After the lift coefficient reaches its maximum negative value, it decays quickly towards zero because the vortex tube vorticity is diffused in the sphere wake. The time averaged lift coefficient (averaged over a time span between $t = 0.8$ and the maximum time 24.5) for all values of v_{maxt} is negative and small ($O(10^{-2})$). As mentioned earlier, the behavior of $C_L(t)$ during the period $0 < t < 0.8$ is influenced by the initial flow perturbation, and thus its value during this initial period is excluded from the averaging process. The root mean square $C_{L,rms}$ of the lift coefficient as a function of time is also linearly proportional to v_{maxt} with $c = 0.7$.

The lift coefficient of the sphere interacting with a single vortex tube as a function of time is also shown as a reference (marked with an asterisk) in figure 8 for Re = 100, $d_{off} = 0$, and $\sigma = 1$ with $v_{maxt} = v_{max} = 0.148$. Figure 8 shows that the lift coefficient of the sphere interacting with a pair of co-rotation vortex tubes as a function of time is approximately the same as that of the sphere interacting with a single vortex tube for the parameters given above if the same total maximum induced velocity is used in both cases. The dependency of this phenomenon on the parameters (d_{off}, σ, and Re) will be discussed in the following subsections.

Figure 9 shows the temporal development of the moment coefficients for the sphere under the same conditions as figure 8.

When the vortex tubes pass the sphere, the front stagnation point on the sphere is shifted above the plane $x = 0$ due to the downwash. This causes higher shear stress in the lower left region compared to the upper left region resulting in a positive (counter-clockwise) torque on the sphere.

The upward shift of the front stagnation point also causes the shear stress to be higher in the top and upper right regions than in the bottom and lower right regions resulting in a negative torque on the sphere. However, the effect of this negative torque is diminished by the shear flow induced by the vortex tubes across the sphere which produces high shear stress at the bottom of the sphere. As a consequence, a net high positive torque acts on the sphere. The maximum positive moment coefficient $C_{M,max}$ occurs at $t = 11.5$. $C_{M,max}$ is approximately linearly proportional to v_{maxt} with $c = 0.11$.

When the vortex tubes approach the sphere or are relatively far away from the sphere, the effect of the shear flow induced by the vortex tubes across the sphere is small, resulting in a net weak torque on the sphere.

The time averaged moment coefficient for all values of v_{maxt} is positive and small $O(10^{-3})$. The rms moment coefficient $C_{M,rms}$ is approximately linearly proportional to v_{maxt} with $c = 0.043$. We note that the torque depends only the distribution of the shear stresses ($\tau_{r\theta}$ and $\tau_{r\phi}$) and is relatively small compared to the lift force.

The moment coefficient of the sphere interacting with a single vortex tube as a function of time is also shown as a reference (marked with an asterisk) in figure 9 for Re = 100, $d_{off} = 0$, and $\sigma = 1$ with $v_{maxt} = v_{max} = 0.148$. The pattern of the moment coefficient of the sphere interacting with a pair of vortex tubes as a function of time is similar to that of the sphere interacting with a single vortex tube for the parameters given above, but the maximum moment coefficient of the former is lower than that of the latter. This shows that the moment coefficient is more sensitive to the offset distance than the lift coefficient. This will be discussed in the next section in detail.

Figure 10 shows the drag coefficients of the sphere as a function of time for the same conditions as figure 8. The drag coefficients are computed for four different values of v_{maxt} as in figure 8, in addition to $v_{maxt} = 0$ which corresponds to the axisymmetric flow without the vortex tubes.

As discussed earlier, the sudden placement of the sphere in the flow results in initially large values of shear stress and pressure on the sphere, and hence a large drag as shown in figure 10. When the vortex tubes approach the sphere, the pressure at the front stagnation point is lower than that of the axisymmetric flow past a sphere due to the low pressure at the center of the vortex tube. Also, the maximum shear stresses in the upper and lower regions of the sphere are lower than those of the axisymmetric flow. This causes the drag on the sphere to be lower than that of the axisymmetric flow without the vortex tube. As the vortex tubes move around the bottom of the sphere, the front stagnation point is shifted above the plane $x = 0$ due to the downwash.

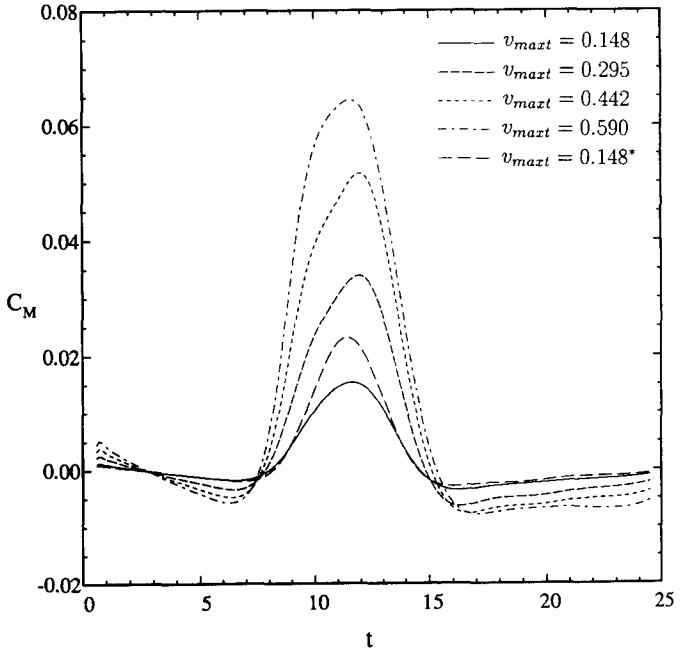

Figure 9. Moment coefficients of the sphere under the same conditions as figure 7.

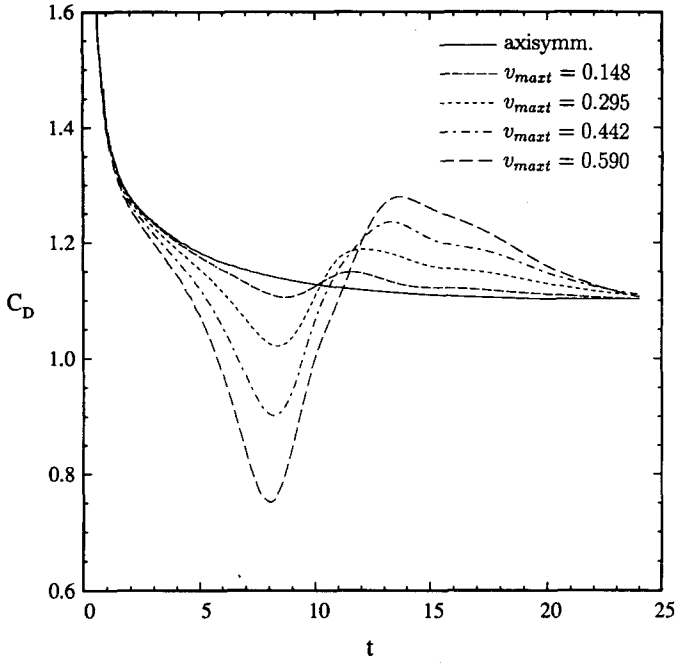

Figure 10. Drag coefficients of the sphere under the same conditions as figure 7.

Consequently, high pressure and high shear stress act in the upper and lower left regions, respectively. This increases the drag during the period $9 < t \leqslant 13.4$. For $t > 13.4$, the drag approaches that of the axisymmetric flow as the vortex tube moves further downstream. The time averaged value of the deviation of the drag coefficient from that of the axisymmetric flow past a sphere for all values of v_{maxt} is nearly zero ($O(10^{-4})$).

The pattern of the drag coefficient of the sphere interacting with a pair of vortex tubes as a function of time is similar to that of the sphere interacting with a single vortex tube for the parameters given above (compared with figure 11 in KES), but the largest deviation of the former from the case of the axisymmedtric flow occurs earlier than that of the latter. The reason is that due to the rotation about each other, one of the vortex tubes in the former approaches the sphere faster than the vortex tube in the latter.

3.3.3. Effects of the size and the offset distance of the vortex tubes. The effects of the size of the vortex tubes on the flow field are studied by performing computations similar to those in the previous section for Re = 100, $d_{off} = \pm 1.5$, and five different sizes of the vortex tubes, $\sigma = 0.25$, 0.5, 2, 3, and 4 in addition to the base case $\sigma = 1$.

Table 1 shows $C_{L,max1}$, $C_{L,max2}$, $C_{L,rms}$, $C_{M,max}$, and $C_{M,rms}$ as a function of the vortex tube size which covers six different initial radii of the vortex tube, $\sigma = 4$, 3, 2, 1, 0.5, and 0.25, for $v_{maxt} = 0.1$. Another computation with different v_{maxt} showed that all the lift and moment coefficients are linearly proportional to v_{maxt} at each σ. When $\sigma \geqslant 2$, $C_{L,max1}$ and $C_{L,rms}$ become *independent* of σ, but the magnitudes of $C_{L,max2}$, $C_{M,max}$, and $C_{M,rms}$ for $\sigma = 4$ are smaller than those for $\sigma = 2$ and 3. When

Table 1. Maximum positive and negative lift coefficients, rms lift coefficient, maximum moment coefficient, and rms moment coefficient as a function of the size of vortex tube for Re = 100 and $d_{off} = 1.5$ with $v_{maxt} = 0.1$

σ	$C_{L,max1}$	$C_{L,max2}$	$C_{L,rms}$	$C_{M,max}$	$C_{M,rms}$
4	0.111	− 0.186	0.103	0.011	0.0051
3	0.111	− 0.196	0.102	0.013	0.0053
2	0.108	− 0.197	0.094	0.013	0.0053
1	0.088	− 0.162	0.070	0.011	0.0043
0.5	0.058	− 0.116	0.046	0.0065	0.0023
0.25	0.034	− 0.070	0.027	0.0034	0.0012

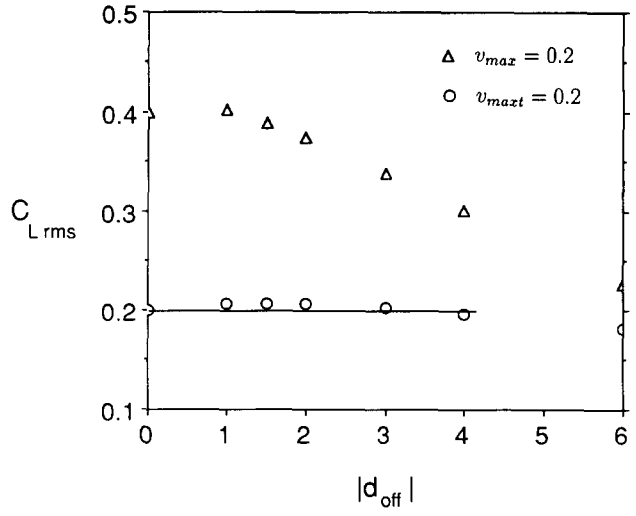

Figure 11. Rms lift coefficients of the sphere as a function of $|d_{off}|$ for Re = 100 and $\sigma = 4$.

σ approaches zero, all the coefficients tend to be proportional to (σv_{maxt}) or (σv_{max}) which is proportional to the *circulation* of the vortex tube. For example, $C_{L,rms}$ is expressed by

$$C_{L,rms} = c_1 v_{maxt}, \qquad 2 \leqslant \sigma \leqslant 4$$

$$= c_2 v_{maxt} \sigma^n, \quad 0.25 \leqslant \sigma < 2, \quad 0.75 \geqslant n \geqslant 0.3, \qquad [7]$$

where the constant $c_1 = 1$ and $c_2 = 0.7$, and n depends on σ and should approach unity as σ reaches zero. For $C_{L,max1}$, $c_1 = 1.1$ and $c_2 = 0.88$. $C_{L,max2}$, $C_{M,max}$, and $C_{M,rms}$ for $\sigma \leqslant 3$ are also expressed by [7] with $c_1 = -2$ and $c_2 = -1.65$, $c_1 = 0.13$ and $c_2 = 0.11$, and $c_1 = 0.053$ and $c_2 = 0.04$, respectively. The time averaged value of the deviation of the drag coefficient from that of the axisymmetric flow past a sphere for all values of σ is nearly zero ($O(10^{-4})$).

Comparing the results in table 1 (based on v_{maxt}) with those of the sphere interacting with a single vortex tube (KES, table 4 (based on v_{max})), it is found that the magnitudes of the lift coefficients in table 1 are within 2–20% of those in KES, with the largest deviation occurring at $\sigma = 0.25$.

Note that $C_{L,max2}$, $C_{M,max}$, and $C_{M,rms}$ for $\sigma = 4$ are, respectively, smaller than those for $\sigma = 2$ and 3 due to the shear flow effect explained in KES.

Now, the effects of the offset distance on the flow field are investigated by varying d_{off} for Re = 100 and $\sigma = 4$. The computation was performed for $d_{off} = 0, \pm 1, \pm 2, \pm 3$, and ± 4 in addition to the base case $d_{off} = \pm 1.5$. Note that the case of $d_{off} = 0$ corresponds to the interaction between a *single* vortex tube and a sphere.

It is found that $C_{L,max1}$, $C_{L,max2}$, $C_{L,rms}$, $C_{M,max}$, and C_{Mrms} for each d_{off} are linearly proportional to v_{maxt} as in the case of $d_{off} = \pm 1.5$. The triangular symbols in figure 11 show $C_{L,rms}$ as a function of $|d_{off}|$ for Re = 100 and $\sigma = 4$ while the maximum induced velocity (or the circulation) of each vortex tube is kept as a constant, $v_{max} = 0.2$. The triangular symbols show that $C_{L,rms}$ decays rapidly as $|d_{off}| > 0$. On the other hand, the circular symbols in figure 11 show $C_{L,rms}$ as a function of $|d_{off}|$ for Re = 100 and $\sigma = 4$ while the total maximum induced velocity due to the two vortex tubes is kept as a constant, $v_{maxt} = 0.2$. The circular symbols show that the magnitudes of the rms lift coefficients for $d_{off} = \pm 1, \pm 1.5, \pm 2, \pm 3$, and ± 4 are close to that for $d_{off} = 0$. The behavior of $C_{L,max1}$ and $C_{L,max2}$ as a function of $|d_{off}|$ is similar to that of $C_{L,rms}$.

Examination of the effect of the offset distance for $\sigma = 1$ and 2 shows that the lift coefficient of the sphere interacting with a pair of vortex tubes as a function of time is nearly identical to that of the sphere interacting with a single vortex tube if the separation distance between the tube centers is less than $2\sqrt{\sigma}$ vortex tube diameter for Re = 100 and v_{maxt} instead of v_{max} is used in the former.

The triangular symbols and the circular symbols in figure 12 show $C_{M,rms}$ as a function of $|d_{off}|$ for the same parameters as used for $C_{L,rms}$. Figure 12 shows that the magnitude of the rms moment

coefficient decays more rapidly than that of the rms lift coefficient as d_{off} increases. The behavior of $C_{M,max}$ as a function of d_{off} is similar to that of $C_{M,rms}$. The moment coefficient of the sphere interacting with a pair of vortex tubes as a function of time is nearly identical to that of the sphere interacting with a single vortex tube if the separation distance between the tube centers is less than $\sqrt{\sigma}$ vortex tube diameter for Re = 100 and v_{maxt} instead of v_{max} is used in the former.

3.3.4. Effects of Reynolds number. Computations like those in section 3.3.2 are made for four different Reynolds numbers in the range of $20 \leqslant \mathrm{Re} \leqslant 80$, $d_{off} = \pm 1.5$, and $1 \leqslant \sigma \leqslant 4$ in addition to the base case Re = 100.

A result like that shown in section 3.3.3 for Re = 100 is obtained. $C_{L,max1}$ and $C_{L,rms}$ are linearly proportional only to v_{maxt} and independent of σ when $\sigma \geqslant 2$ at fixed Reynolds number as in the case of Re = 100. $C_{L,max1}$ dependence on Reynolds number may be expressed by

$$C_{L,max1} = A v_{maxt} \mathrm{Re}^{P}, \qquad [8]$$

where $A = 8.9$ and $P = -0.45$ for $2 \leqslant \sigma \leqslant 4$. $C_{L,rms}$ may be also expressed by [8] with $A = 8.1$ and $P = -0.45$ for $2 \leqslant \sigma \leqslant 4$. $C_{M,max}$ and $C_{M,rms}$ may be also represented by [8] with $A = 5.5$ and $P = -0.83$ for the former, and $A = 3.1$ and $P = -0.88$ for the latter for $2 \leqslant \sigma \leqslant 3$.

Now, the effect of the offset distance for $20 \leqslant \mathrm{Re} \leqslant 80$ in addition to the base case Re = 100 is discussed.

The triangular symbols in figure 13 show $C_{L,rms}$ as a function of $|d_{off}|$ for Re = 20 and $\sigma = 4$ while the maximum induced velocity (or the circulation) of each vortex tube is kept as a constant, $v_{max} = 0.2$. The triangular symbols show that $C_{L,rms}$ decays rapidly as $|d_{off}| > 0$. On the other hand, the circular symbols show $C_{L,rms}$ as a function of $|d_{off}|$ for Re = 20 and $\sigma = 4$ while the total maximum induced velocity due to the two vortex tubes is kept as a constant, $v_{maxt} = 0.2$. The circular symbols show that the magnitudes of the rms lift coefficients for $d_{off} = \pm 2$ and ± 4 are close to that for $d_{off} = 0$. The behavior of $C_{L,max1}$ and $C_{L,max2}$ as a function of $|d_{off}|$ resembles that of $C_{L,rms}$.

The results for the range of σ values indicate that the lift coefficient of the sphere interacting with a pair of co-rotation vortex tubes as a function of time is nearly identical to that of the sphere interacting with a single vortex tube if the separation distance between the tube centers is less than $2\sqrt{\sigma}$ vortex tube diameter for Re = 20 and v_{maxt} instead of v_{max} is used in the former case. The same result as above was obtained at different Reynolds numbers, Re = 40, 60, and 80.

The triangular symbols and the circular symbols in figure 14 show $C_{M,rms}$ as a function of $|d_{off}|$ for the same parameters as used for $C_{L,rms}$. The figure shows the magnitude of the rms moment coefficient decays more rapidly than that of the rms lift coefficient as d_{off} increases. The behavior of $C_{M,max}$ as a function of d_{off} resembles that of $C_{M,rms}$. It is found that the moment coefficient of the sphere interacting with a pair of vortex tubes as a function of time is nearly identical to that of the sphere interacting with a single vortex tube if the separation distance between the tube centers is less than $\sqrt{\sigma}$ vortex tube diameter for Re = 20 and v_{maxt} instead of v_{max} is used in the former case. The same result as above was obtained at different Reynolds numbers, Re = 40, 60, and 80.

3.4. Interactions of an array of vortex tubes of co-rotation and a moving sphere

Our results for the cases of a fixed spherical particle interacting with a single advecting vortex and with an advecting pair of vortices can now be used to calculate the trajectory of a moving spherical particle interacting with an array of co-rotating vortex tubes. Counter-rotating vortices are less interesting since they produce no lift or deflection. Studying these interactions can improve our understanding of the behavior of a particle (or droplet) interacting with eddies of comparable length scale in a turbulent flow. For this study, the array will be a linear arrangement of single vortices. Since a single vortex and a pair of co-rotating vortices produce comparable effects on the sphere, this choice should not be critical.

Figure 15 shows the initial flow geometry where a spherical particle is injected into an array of infinite number of counter-clockwise rotating vortices which are located on the negative z-axis with center-to-center nondimensional distance of 24. Since the life time of a vortex tube is short ($2\pi\sigma/v_{max}$) compared to the travel time (or life time) of the particle (or droplet), it is assumed that the next vortex with the same strength as the first vortex is generated when the sphere passes the

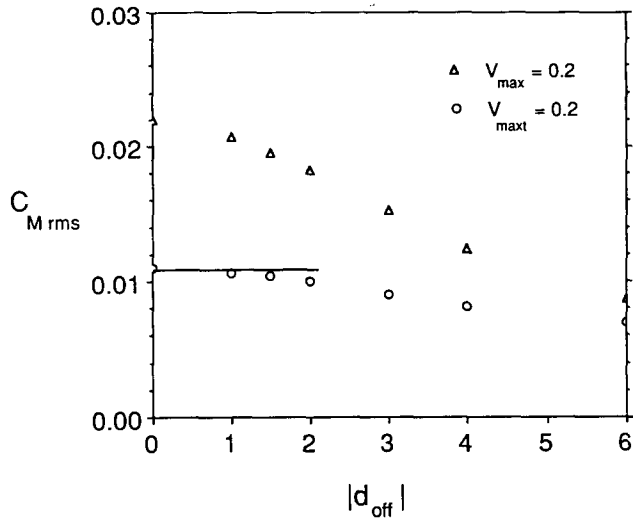

Figure 12. Rms moment coefficients of the sphere as a function of $|d_{off}|$ for Re = 100 and $\sigma = 4$.

first vortex. The deflection of the moving sphere will cause the offset distance to vary from one collision with a vortex tube to the next. Therefore, d_{off} is a time-dependent quantity.

We assume that the particle is constrained to move only in the x–z plane. The aim is to calculate the trajectory in the two-dimensional plane from the already-known time evolution of $C_D(t)$ and $C_L(t)$ as given by KES. The particle trajectory as a function of time is computed by solving the following system of two ordinary differential equations which are the nondimensional form of the Newton's equation of motion in the z and x directions

$$\frac{dU_z}{dt} = \frac{3}{8\rho_r}(-C_D(t)\cos\theta - C_L(t)\sin\theta)(U_z^2 + U_x^2) \quad [9a]$$

$$\frac{dU_x}{dt} = \frac{3}{8\rho_r}(-C_D(t)\sin\theta + C_L(t)\cos\theta)(U_z^2 + U_x^2), \quad [9b]$$

where U_z and U_x are, respectively, the sphere velocities in the z and x directions, $\tan\theta = U_x/(-U_z)$, and ρ_r is the ratio of the particle density to the fluid density. Initially, $\theta = 0$. The term $(U_z^2 + U_x^2)$ arises since the velocities are normalized by the initial particle velocity while the drag and lift coefficients are normalized by the instantaneous particle velocity. The gravity force is neglected in this formulation.

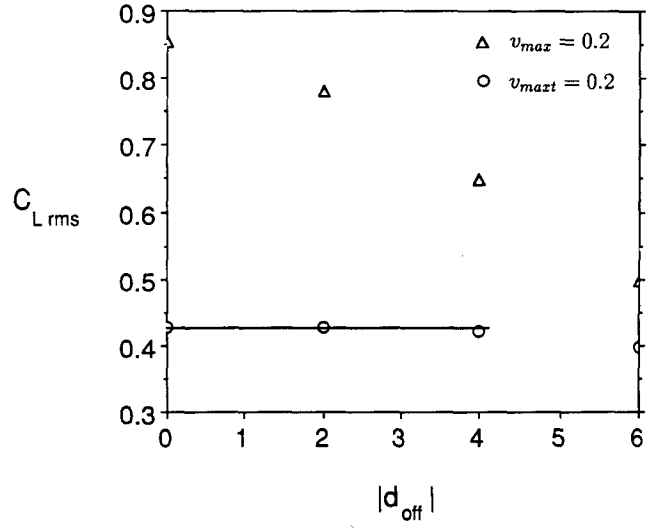

Figure 13. Rms lift coefficients of the sphere as a function of $|d_{off}|$ for Re = 20 and $\sigma = 4$.

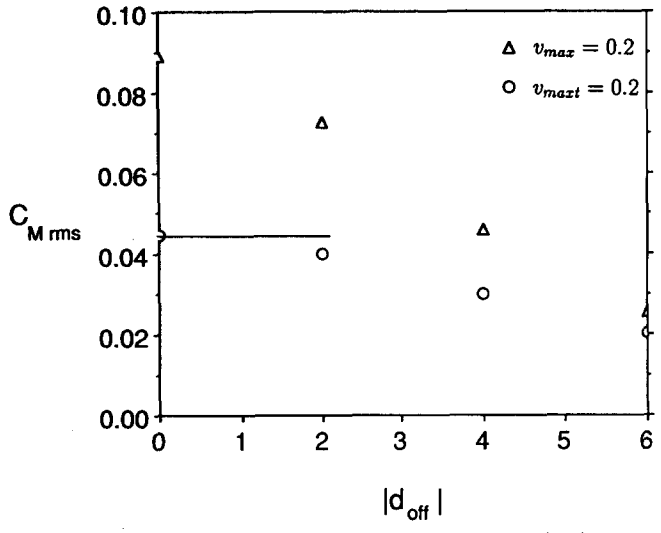

Figure 14. Rms moment coefficients of the sphere as a function of $|d_{off}|$ for Re = 20 and $\sigma = 4$.

Our numerical results (KES) for the time-dependent lift coefficient of a spherical particle interacting with a single vortex tube depends on the offset distance d_{off}, the vortex core size σ, and Reynolds number Re and can be summarized as:

$$C_L(t) = A[C_L(t)]_b \exp\left(\frac{Bd_{off}}{\sqrt{\sigma}}\right) f(\mathrm{Re}, v_{max}) \quad \text{for } C\sqrt{\sigma} \leqslant d_{off} \leqslant D\sqrt{\sigma}, \qquad [10]$$

where the following combinations of values apply (table 2).

Table 2.

A	B	C	D
1.15	0.3	$-\infty$	-0.7
1	0.1	-0.7	0
1	0	0	1
$e^{0.1}$	-0.1	1	1.7
$1.15e^{0.3}$	0.3	1.7	∞

Also, $[C_L(t)]_b$ is the lift coefficient for the base case where Re = 100 and $d_{off} = 0$ with $v_{max} = v_{max,b}$, $f(\mathrm{Re}, v_{max}) = (100/\mathrm{Re})^m v_{max}/v_{max,b}$, and the exponent m is given by table 3.

Table 3.

m	σ	t
0.375	1	$0 \leqslant t \leqslant 9$
0.45	1	$9 < t \leqslant 24$
0.44	$2 \leqslant \sigma \leqslant 4$	$0 \leqslant t \leqslant 9$
0.51	$2 \leqslant \sigma \leqslant 4$	$9 < t \leqslant 24$

The time-averaged drag coefficient of the sphere in the flow with a vortex tube differs by 0.01–5% (depending on the offset distance) from the time-averaged drag coefficient of the axisymmetric flow for Re = 100 and $v_{max} = 0.2$. (Refer to [19] in KES.) Therefore, the time-dependent drag coefficient in [9a] and [9b] is approximated by the time-dependent drag coefficient obtained from the axisymmetric flow generated by a spherical particle injected into a quiescent fluid. The spherical particle in this flow experiences the drag force and thus is retarded. This axisymmetric drag coefficient was computed as a function of time and instantaneous Reynolds number by using the code which has been developed for the time-dependent axisymmetric flow. The torque on the sphere is neglected since the magnitude of the moment coefficient is small and less than 8% of the lift coefficient magnitude (table 4 of KES).

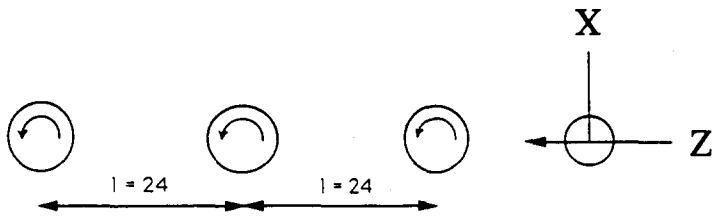

Figure 15. Initial flow geometry for a sphere injected into an array of infinite number of vortex tubes.

Figure 16 shows two trajectories of the sphere during the dimensionless time period between 0 and 24 for initial particle Reynolds numbers 50 and 100 with density ratio 200 (which is the ratio, for example, of n-octane density to that of air under 10 atmospheres of pressure). The initial vortex size is three times the sphere radius, and the initial offset distance of the sphere is zero. The initial maximum induced velocity of the vortex tube is 0.2 normalized by the initial sphere velocity. The sphere initially moves upward due to the vortex upwash and then moves downward due to the vortex downwash. The maximum positive deflection for the case of $Re_0 = 50$ is higher than that of $Re_0 = 100$.

Figure 17 shows two trajectories of the sphere which are traced from the initial injection beyond the time period of figure 16 until particle Reynolds number reaches unity for initial particle Reynolds numbers 50 and 100 with the same initial parameters as in figure 16. Since the final Reynolds number is small, these trajectories are approximately those corresponding to the whole particle motion until it stops relative to the fluid. A counter-clockwise rotating vortex tube produces not only upwash downstream of itself and downwash upstream of itself but it also causes a shear flow across the sphere when it passes the sphere. The combined effect of the downwash and the shear flow causes the magnitude of the maximum negative lift to be greater than the maximum positive lift magnitude. Therefore, the average lift coefficient averaged over the time span 24 (the interaction time with one vortex tube) is one order of magnitude less than the rms lift coefficient and negative due to the shear flow effect. This small negative value of the average lift coefficient becomes important when the sphere interacts with an array of many vortices. Thus, the sphere travels upward only for the short initial time period and then moves downward for the most of the time until it stops. The final deflection ratios defined by the ratio of the final position x_f to z_f of the sphere are 1/36 for the case of $Re_0 = 100$ and 1/34 for the case of $Re_0 = 50$. However, the final deflection for the case of $Re_0 = 100$ is higher than that of $Re_0 = 50$, because the sphere for the case of $Re_0 = 100$ possesses higher initial momentum and it travels farther than that of $Re_0 = 50$.

Figure 18 shows four trajectories of the sphere during the dimensionless time period between 0 and 24 for the density ratio 25, 50, 100, and 200 with Reynolds number 100 and the same parameters for σ, d_{off}, and v_{max} as in figure 16. A sphere with lower density ratio initially deflects more than a sphere with higher density ratio as shown in figure 18. Figure 19 shows four trajectories

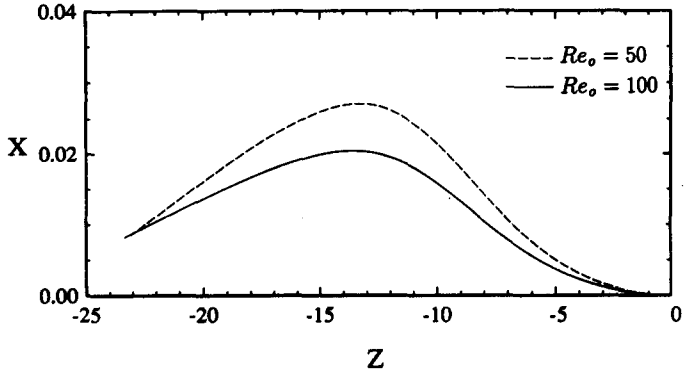

Figure 16. Two trajectories of the sphere during the time period between 0 and 24 for initial Reynolds numbers 50 and 100 with density ratio 200.

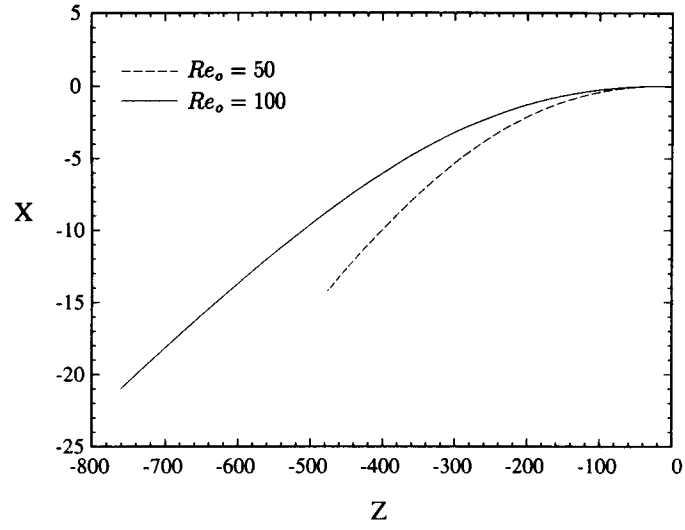

Figure 17. Two trajectories of the sphere traced from the initial injection until Reynolds number reaches unity for initial Reynolds numbers 50 and 100 with density ratio 200.

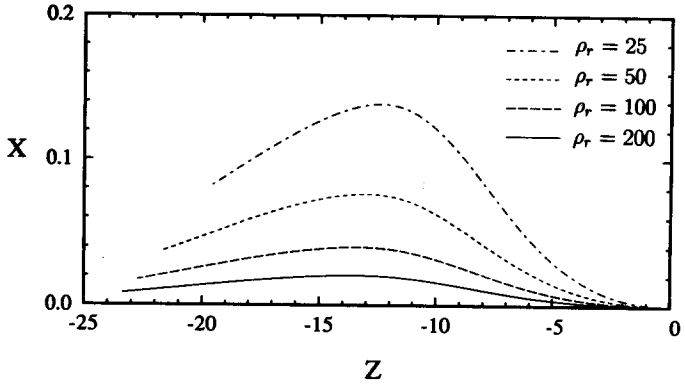

Figure 18. Four trajectories of the sphere during the time period between 0 and 24 for the density ratio 25, 50, 100, and 200 with initial Reynolds number 100.

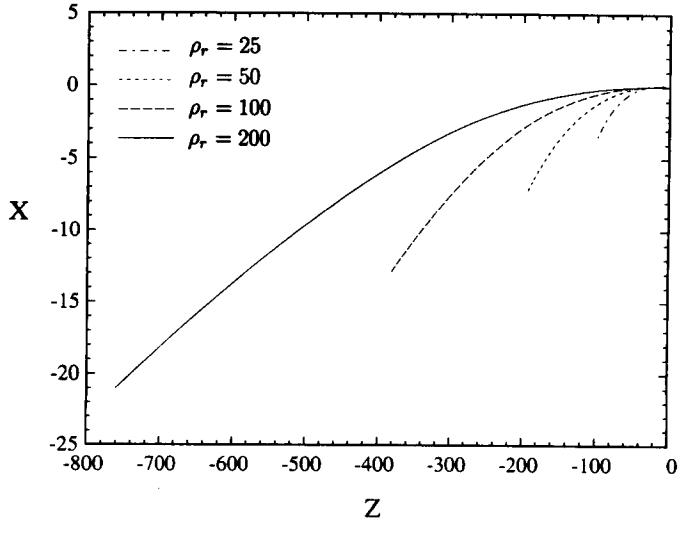

Figure 19. Four trajectories of the sphere traced from the initial injection until Reynolds number reaches unity for the density ratios 25, 50, 100, and 200 with initial Reynolds number 100.

of the sphere which are traced from the initial injection until particle Reynolds number reaches unity for the density ratio 25, 50, 100, and 200 with the same initial parameters as in figure 18. However, the final transverse displacement increases with density ratio because the sphere with higher density ratio possesses higher initial momentum and it travels farther than the sphere with lower density ratio.

The larger v_{max} causes the larger sphere deflection; however, the sphere deflection is not linearly proportional to v_{max} due to the nonlinearity of [9a] and [9b].

The results of figures 16 and 18 indicate that the sphere would experience slightly lower drag than that of a sphere subjected to an axisymmetric flow when it passes the first vortex tube. This lower drag is caused by the upward motion of the sphere due to the upwash of the approaching vortex tube, and thus the center of the vortex tube is located below the front stagnation point of the sphere. This causes lower dynamic pressure ahead of the front stagnation point. However, the sphere would experience higher drag eventually when it passes more than one vortex tube and travels downward. Due to the downward motion, the vortex tubes are located above the front stagnation point of the sphere, causing higher dynamic pressure ahead of the front stagnation point.

The original computations in KES and in section 3.3 were made for a nondimensional time duration of 24 and 24.5, respectively. However, the trajectory calculations presented in figures 17 and 19 use the basic information from those original computations to yield trajectory predictions for much longer periods.

4. CONCLUSIONS

In order to improve the understanding of the physics of interaction between a particle and eddies of comparable length scale in a carrier flow, the unsteady, three-dimensional, incompressible, viscous flow interactions between a pair of vortex tubes advected by a uniform free stream and a spherical particle suddenly placed and held fixed in space were investigated numerically for a range of particle Reynolds number $20 \leqslant \mathrm{Re} \leqslant 100$.

When the top and bottom vortex tubes have positive and negative circulations, respectively, the magnitude of the induced velocity due to the vortex tubes is added to the base flow velocity along the stagnation streamline. This causes the pressure at the stagnation point and the shear stresses in the upper and lower left regions to be higher than those of the axisymmetric flow past a sphere, thus increasing the drag. On the other hand, when the top and bottom vortex tubes have negative and positive circulations, respectively, the induced velocity due to the vortex tubes is subtracted from the base flow velocity along the stagnation streamline. This causes the pressure at the stagnation point and the shear stresses in the upper and lower left regions to be lower than those of the axisymmetric flow past a sphere, thus reducing the drag. The lift and moment are zero for this symmetric configuration.

The interactions between a sphere and a pair of co-rotating cylindrical vortex tubes initially located ten radii upstream from the center of the sphere were investigated. The lift and moment coefficients of the sphere interacting with a pair of vortex tubes as a function of time are nearly identical, respectively, to those of the sphere interacting with a single vortex tube if the separation distance between the tube centers is less than $2\sqrt{\sigma}$ vortex tube diameter for the lift coefficient and less than $\sqrt{\sigma}$ vortex tube diameter for the moment coefficient; here, v_{maxt} instead of v_{max} is used in the case of a pair of vortex tubes, where v_{max} is the maximum induced velocity due to one vortex without presence of the other and v_{maxt} is the total maximum induced velocity due to the pair of vortices. In particular, lift and moment coefficients are linearly proportional to the maximum induced velocity. The moment coefficient is negligible compared to the lift coefficient.

The two-dimensional trajectories of a spherical particle interacting with an array of vortices whose sizes are comparable to the sphere size have been examined. The time-dependent drag and lift forces (KES) for the case of a spherical particle interacting with a single vortex were used to calculate the two-dimensional trajectory of a moving spherical particle interacting with an array of vortex tubes of co-rotation. The present results show that the shear flow across the sphere induced by a vortex tube is responsible for the net deflection of a sphere interacting with an array of vortex tubes. Thus, the sphere eventually deflects in the direction of increasing relative velocity. The deflection ratio (ratio of sphere final location in the z and x directions) of the sphere increases with decreasing initial Reynolds number and with decreasing density ratio. However, the total

deflection increases with increasing the initial Reynolds number and the density ratio because higher momentum causes the sphere to travel farther.

The temporal variations of C_L, C_M, and C_D (figures 8–10) indicate that a significant change in C_L, C_M, and C_D occurs only when the vortices are in the proximity of the sphere, otherwise they remain nearly negligible. This result will be the same for the case of a particle drifting with its terminal velocity and interacting with the same vortices. That is, the start-up transient during the first few residence times does not affect this interaction because the computations begin with the vortices far upstream.

Acknowledgements—This work has been supported by the Air Force Office of Scientific Research under grant No. F49620-93-1-0028 with Dr Julian Tishkoff acting as the technical monitor. We would like to thank Mr Lyle Wiedeman for his assistance in using a three-dimensional graphic package Application Visualization System (AVS). The support of the San Diego Supercomputer Center and the San Diego Supercomputer Center under a block grant of the Office of Academic Computing of UCI are gratefully appreciated.

REFERENCES

Anderson, D. A., Tannehill, J. C. and Pletcher, R. H. (1984) *Computational Fluid Mechanics and Heat Transfer*. Hemisphere Publishing, New York.

Birouk, M., Chauveau, C., Sarh, B., Quilgars, A. and Gökalp, I. (1996) Turbulence effects on the vaporization of monocomponent single droplets. *Combust. Sci. Tech.* **113–114,** 413–428.

Chung, J. N. and Troutt, T. R. (1988) Simulation of particle dispersion in an axisymmetric jet. *J. Fluid Mech.* **186,** 199–222.

Crowe, C. T., Chung, J. N. and Trout, T. R. (1988) Particle mixing in free shear flows. *Prog. Energy Combust. Sci.* **14,** 171–194.

Kim, I., Elghobashi, S. and Sirignano, W. A. (1995) Unsteady flow interactions between an advected cylindrical vortex tube and a spherical particle. *J. Fluid Mech.* **288,** 123–155.

Kim, I., Elghobashi, S. and Sirignano, W. A. (1996) The motion of a spherical particle in unsteady flows at moderate Reynolds Numbers. *34th AIAA Aerospace Sciences Meeting*, Preprint 96-0081.

Martin, J. E. and Meiburg, E. (1994) The accumulation and dispersion of heavy particles in forced two-dimensional mixing layers. *Phys. Fluids* **3,** 1116–1132.

Overman, E. A. and Zabusky, N. J. (1982) Evolution and merger of isolated vortex structures. *Phys. Fluids* **25,** 1297–1305.

Patnaik, G. (1986) A numerical solution of droplet vaporization with convection. Ph.D. dissertation, Carnegie-Mellon University.

Patnaik, G., Sirignano, W. A., Dwyer, H. A. and Sanders, B. R. (1986) A numerical technique for the solution of a vaporizing fuel droplet. *Prog. Astro. Aero.* **105,** 253–266.

Rangel, R. and Sirignano, W. A. (1989) The dynamics of vortex pairing and merging. *27th AIAA Aerospace Sciences Meeting*, Preprint 89-0128.

Spalart, P. R. (1982) Numerical simulation of separated flows. Ph.D. thesis, Stanford University.

Tang, L., Wen, F., Yang, Y., Crowe, C. T., Chung, J. N. and Troutt, T. R. (1992) Self-organizing particle dispersion mechanism in a plane wake. *Phys. Fluids A* **4,** 2244–2251.

Vinokur, M. (1983) On one-dimensional stretching functions for finite-difference calculations. *J. Comput. Phys.* **50,** 215–234.

Zabusky, N. J., Hughes, M. and Roberts, K. V. (1979) Contour dynamics for the Euler equations in two dimensions. *J. Comp. Phys.* **30,** 96–106.